

Supporting information for:

Alloying electrode coatings towards better magnesium batteries

Clément Pechberty,^{1,4} Arthur Hagopian,^{1,4} Jean-Bernard Ledeuil,^{2,4} Dominique Foix,^{2,4} Joachim Allouche,^{2,4} Jean-Noël Chotard,^{3,4} Olivera Lužanin,^{5,6} Jan Bitenc,⁵ Robert Dominko^{5,6,7}, Rémi Dedryvère,^{2,4,7} Jean-Sébastien Filhol,^{1,4} Lorenzo Stievano,^{1,4,7} Romain Berthelot^{1,4,7} *

1 : ICGM, Univ Montpellier, CNRS, ENSCM, Montpellier, France

2 : IPREM, E2S-UPPA, CNRS, Univ. Pau & Pays Adour, Pau, France

3 : LRCS, CNRS UMR7314 Université de Picardie Jules Verne, HUB de l'Energie, 15 rue Baudelocque, 80039 Amiens, France

4 : Réseau sur le Stockage Electrochimique de l'Energie (RS2E), CNRS FR3459, HUB de l'Energie, 15 rue Baudelocque, 80039 Amiens, France

5: Department of Materials Chemistry, National Institute of Chemistry, Hajdrihova 19, 1000 Ljubljana, Slovenia

6: Faculty of Chemistry and Chemical Technology, University of Ljubljana, Večna Pot 113, 1000 Ljubljana, Slovenia

7 : Alistore-ERI, CNRS FR 3104, Hub de l'Energie, Rue Baudelocque 80039 Amiens, France

Corresponding author

Dr. Romain Berthelot

romain.berthelot@umontpellier.fr

Institut Charles Gerhardt de Montpellier (CNRS, UM, ENSCM)

Pôle Chimie Balard – 1919, route de Mende, 34293 Montpellier cedex 5 – France

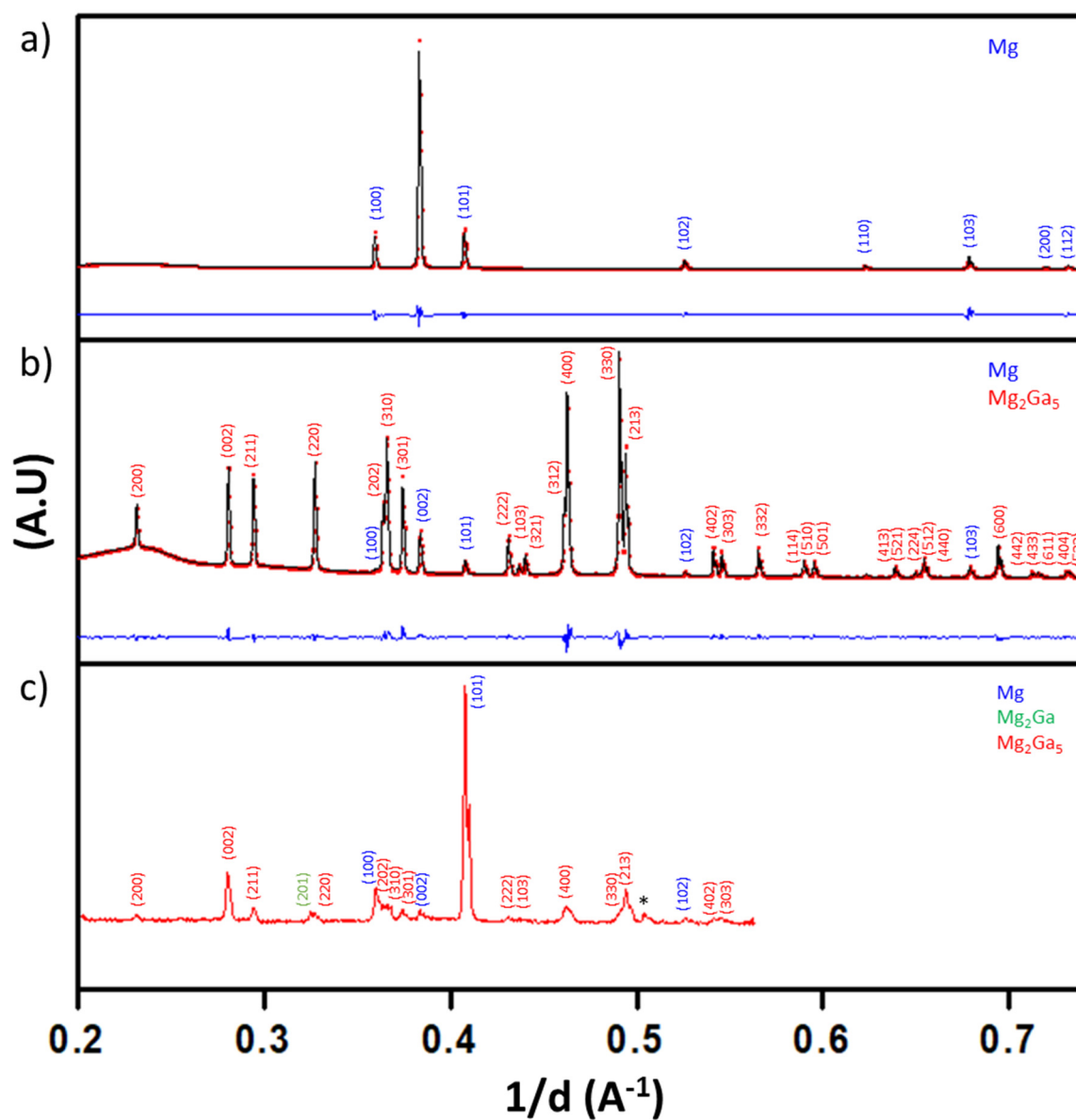


Figure S1. X-ray diffraction patterns of bare Mg and Ga-treated Mg in reflection geometry using Cu-K α radiation and their corresponding profile matching (a and b, respectively), and Ga-coated Mg in transmission geometry using Mo-K α radiation. Miller indices of Mg, Mg_2Ga_5 and Mg_2Ga are in blue, red and green, respectively.

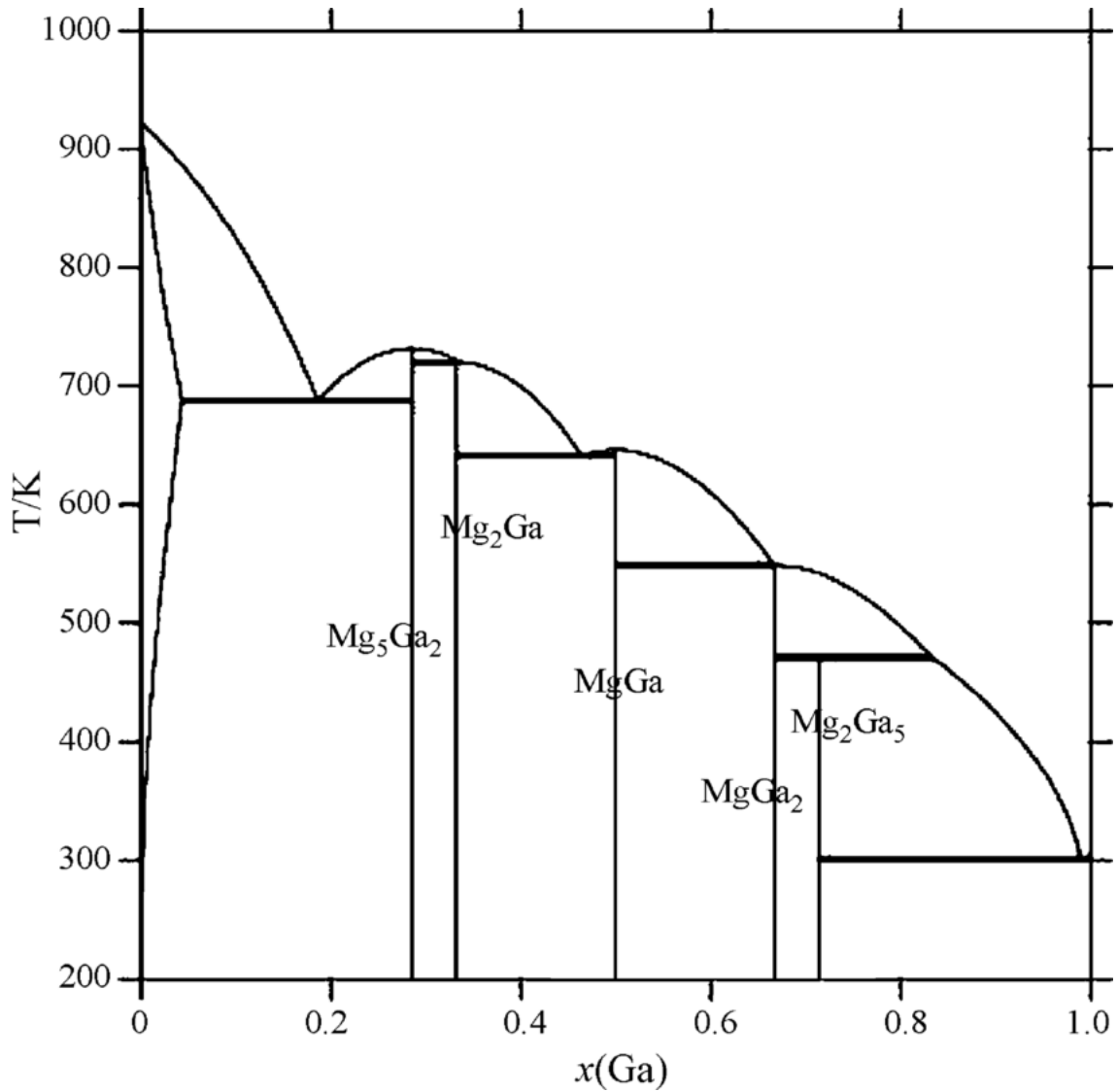


Figure S2: Equilibrium phase diagram of Mg-Ga binary system

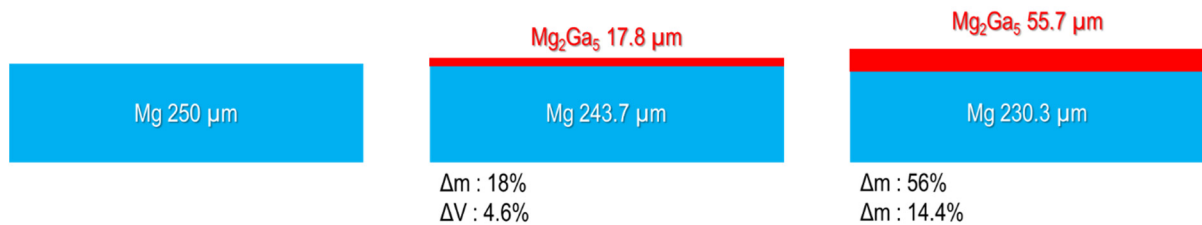


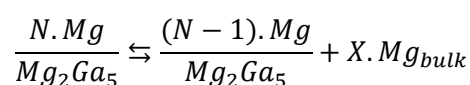
Figure S3. Simplified 2D representation of a Ga-treated magnesium electrode with the experimental mass uptakes ranging from 18 to 56 %. For calculation, it was assumed that only Mg₂Ga₅ was formed. Volumetric mass of Mg and Mg₂Ga₅ were set at 1.74 g/cm³ and 4.98 g/cm³, respectively.

Coating	Electrolyte	Conditions	Observations (overpotential, cycles number)	Ref.
cPAN + Mg triflate	APC	0.01 mA/cm ²	0.05 V for 200h	1
	Mg(TFSI) ₂ /PC (0.5M)	0.01 mA/cm ²	0.5 V for 1000h	
SnCl ₂ /DME drops	Mg(TFSI) ₂ /DME (0.5M)	6 mA/cm ²	0.5V for 3500h	2
GeCl ₄ additive electrolyte	Mg(TFSI) ₂ (0.5M) + (0.4M) GeCl ₄ /DME	10 mA/cm ²	0.25V for 400h	3
BiCl ₃ /DME immersion	Mg(TFSI) ₂ /DME (0.5M)	1 mA/cm ²	0.6V for 4000h	4
LiTFSI + AlCl ₃ Immersion	Mg(TFSI) ₂ /DME (0.5M)	0.01 mA/cm ²	0.3V for 1000h	5
	Mg(TFSI) ₂ /PC (0.5M)		0.2V for 15h	
	Mg(ClO ₄) ₂ /DME (0.5M)		0.6V for 60h	
H ₃ PO ₄ /DME + SiCl ₄ /DME Immersion	Mg(TFSI) ₂ /DME (0.5M)	0.1 mA/cm ²	0.25V for 700h	6
This work	Mg(TFSI)₂/DME (0.8M)	0.1 mA/cm²	0.5V for 200h	

Table S1: Summary of the magnesium plating/stripping experiments reported so far with different strategies and protocols for protecting the magnesium surface

Computational details. Periodic calculations were performed within the density functional theory (DFT) framework, using the Vienna ab initio simulation package (VASP).⁷ The electronic wave functions have been expanded in a plane-wave basis set with a kinetic energy cutoff up to 450 eV. Projector augmented wave (PAW) pseudopotentials were used as implemented in VASP.⁸ Exchange-correlation effects have been accounted for by the generalized gradient approximation (GGA) using the functional of Perdew, Burke and Ernzerhof (PBE).⁹ Convergence criterion has been set to 1.10^{-5} eV for the electronic self-consistent iterations. The structural relaxation was performed until the maximum force on any atom was below 2.10^{-2} eV.Å⁻¹. For Mg₂Ga₅ bulk calculations, the Brillouin zone integration in k-space was performed on a $8 \times 8 \times 10$ Γ -centred Monkhorst-Pack k-point grid.¹⁰ Surface calculations were performed on Mg₂Ga₅ (100), (010) and (001) slabs with 7, 9 and 7 atomic layers, respectively. Mg diffuses more slowly in the coating than into the electrolyte. Therefore, during plating, Mg ions should always accumulate on the coating surface. For that reason, as we focused on the plating process, only Mg surface terminations were considered in the calculations. Cells were built symmetric in the z-direction which is a necessary condition for a proper calculation of surface energetics on polyatomic materials. Bottom and upper layers were allowed to relax while the central layer was kept frozen to avoid interaction through strain of the two slab surfaces. To avoid interaction between periodic images of the slab, a vacuum layer of 20 Å has been set in the z-direction. This allowed to collapse the three-dimensional k-point grid to a planar grid which has been reduced to $8 \times 10 \times 1$, $10 \times 8 \times 1$ and $8 \times 8 \times 1$ for Mg₂Ga₅ (100), (010) and (001) surfaces, respectively. The surrounding surface environment was described with an implicit solvent by using the polarizable continuum model (PCM) as implemented in VASPsol.¹¹ The dielectric constant ($\epsilon_r = 7.2$) of dimethoxyethane (DME) was used. To avoid numerical instabilities, the effective surface tension parameter τ has been set to 0 eV.Å^{-2} , and the cutoff charge density parameter n_c has been set to 5.10^{-5} Å^{-3} .¹² The cavity diffusion parameter has been set to the default value, 0.6. Some surface calculations were done at various applied potentials.

The plating energy (ΔE_p) is defined by the following chemical equilibrium, assuming an initial epitaxial growth of Mg over the Mg_2Ga_5 substrate,



where $\frac{N \cdot Mg}{Mg_2Ga_5}$ and $\frac{(N-1) \cdot Mg}{Mg_2Ga_5}$ correspond to the Mg_2Ga_5 (001) surface covered by N and (N-1) layers of Mg, respectively. X is the number of Mg atoms in the newly adsorbed layer and Mg_{bulk} corresponds to the Mg bulk structure. A negative ΔE_p indicates that the Mg N-layer would thermodynamically convert into a thinner (N-1)-layers with the equivalent number of Mg atoms in its bulk phase, which means, at the interface coating/electrode or into the electrode bulk phase. A negative ΔE_p therefore justify for an underneath plating process.

To compute the adsorption energy E_{ads} of Mg layers on the Mg_2Ga_5 (001) surface, the following relation has been used

$$E_{ads} = E_{Mg_2Ga_5}^{N \cdot Mg} - E_{Mg_2Ga_5} - E_{N \cdot Mg}$$

where $E_{Mg_2Ga_5}^{N \cdot Mg}$, $E_{Mg_2Ga_5}$ and $E_{N \cdot Mg}$ correspond to the energy of the whole interface (N Mg layers adsorbed on the Mg_2Ga_5 (001) surface), of the Mg_2Ga_5 (001) surface without the adsorbed layer, and of the adsorbed Mg layer without the Mg_2Ga_5 (001) surface, respectively.

The stress energy E_{str} that the Mg layer experiences, which is associated to its adsorption on the Mg_2Ga_5 (001) surface, can be related to the polymorphic transition energy E_{poly} and to the epitaxial strain energy E_{epi} following

$$E_{str} = E_{poly} + E_{epi}$$

Where

$$E_{poly} = E_{Mg(h)} - E_{Mg(14/mmm)}$$

With $E_{Mg(14/mmm)}$ and $E_{Mg(h)}$ the energy of a Mg atom relaxed in the crystallographic environment $14/mmm$ of Mg_2Ga_5 , and in its hexagonal phase, respectively, and where

$$E_{epi} = E_{Mg}^{constrained} - E_{Mg}^{relaxed}$$

with $E_{Mg}^{constrained}$ the energy of a Mg atom constrained on x and y coordinates to the Mg_2Ga_5 (001) surface lattice parameters, and with a minimum strain on z coordinate, and with $E_{Mg}^{relaxed}$ the energy of the relaxed slab.

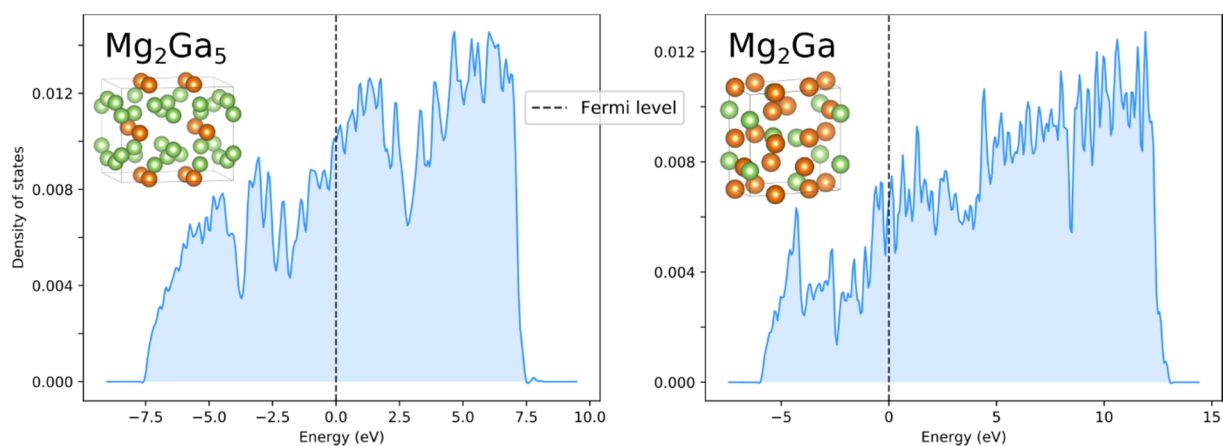


Figure S4. Density of states of Mg_2Ga_5 and Mg_2Ga obtained by DFT calculation.

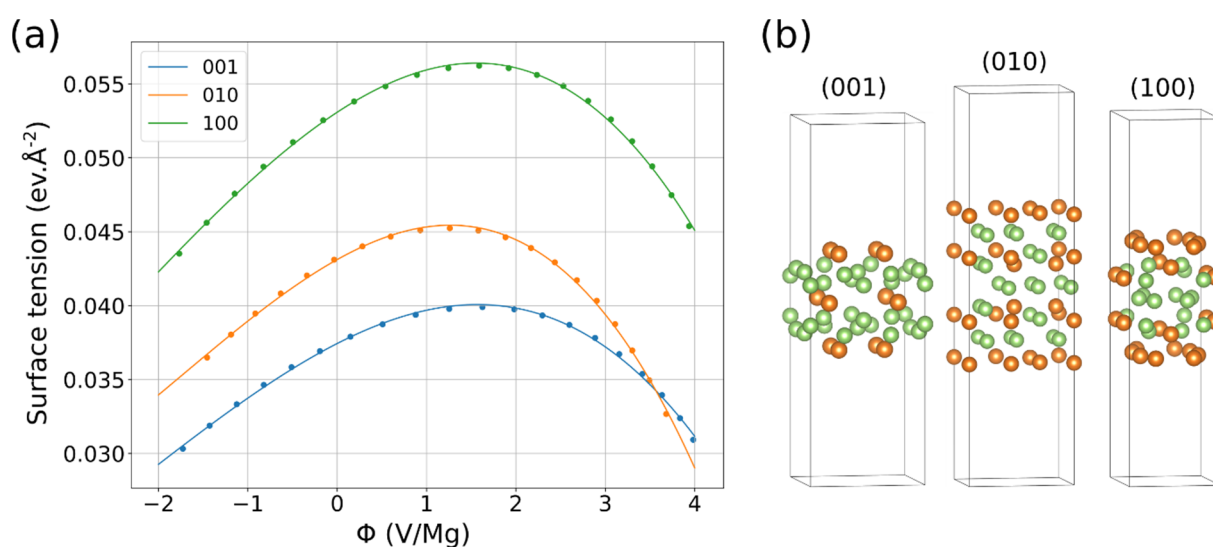


Figure S5: Surface tension as a function of the applied potential for the (001), (010) and (100) Mg_2Ga_5 surfaces in contact with an implicit solvent.

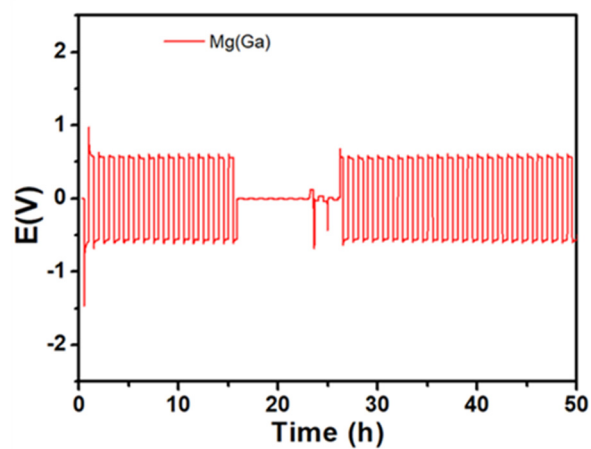


Figure S6. Typical development of overpotentials of galvanostatic polarization measured at room temperature, showing more frequent cell failure by short-cut than at 40 °C.

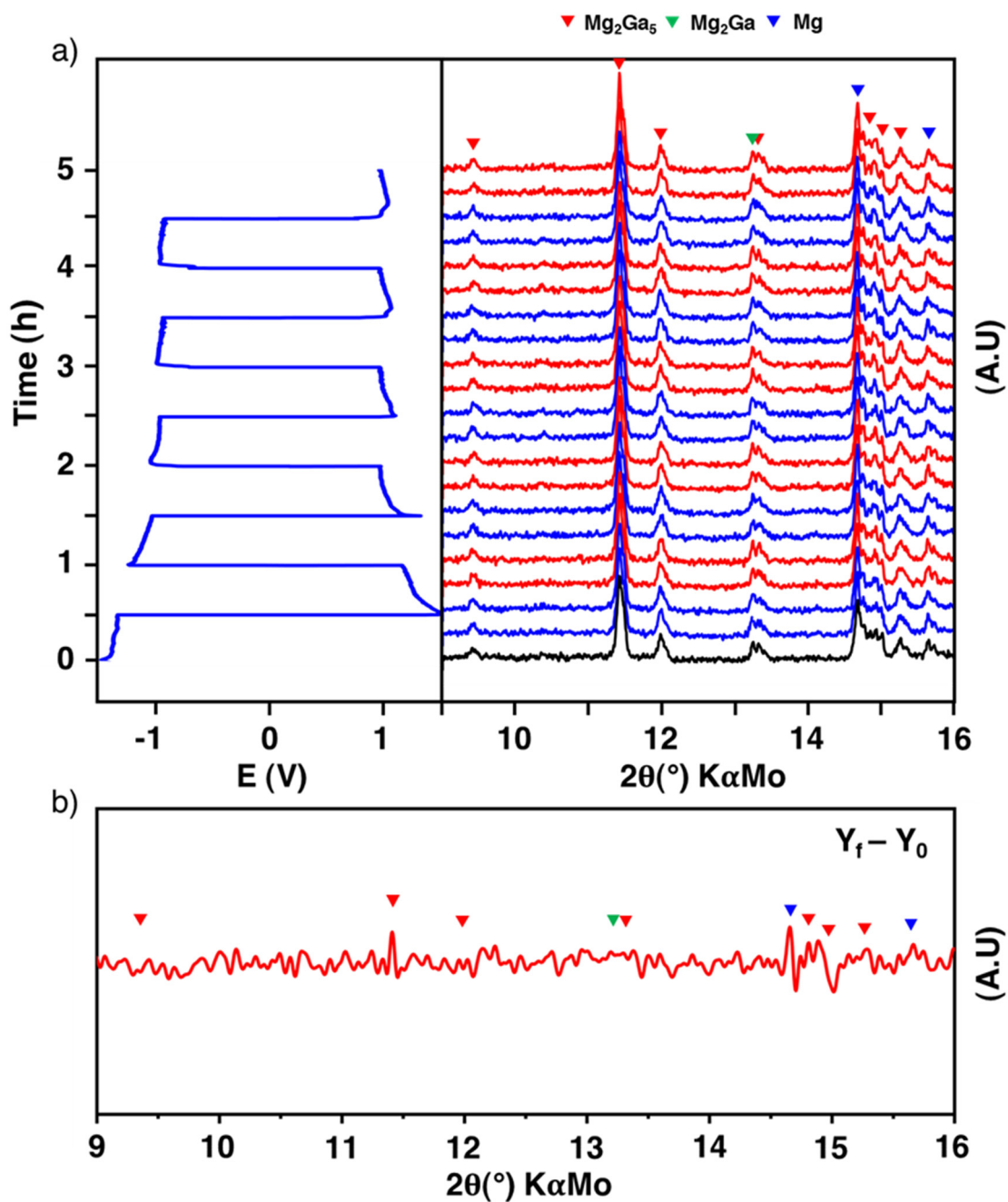


Figure S7. Operando XRD in transmission geometry of polarization test performed at room temperature on a symmetrical cell Mg(Ga)/Mg(Ga) symmetric cell, with galvanostatic profile and raw diffraction patterns (a) and the difference between the last and the first pattern to emphasize any change in the peaks shape and/or width (b).

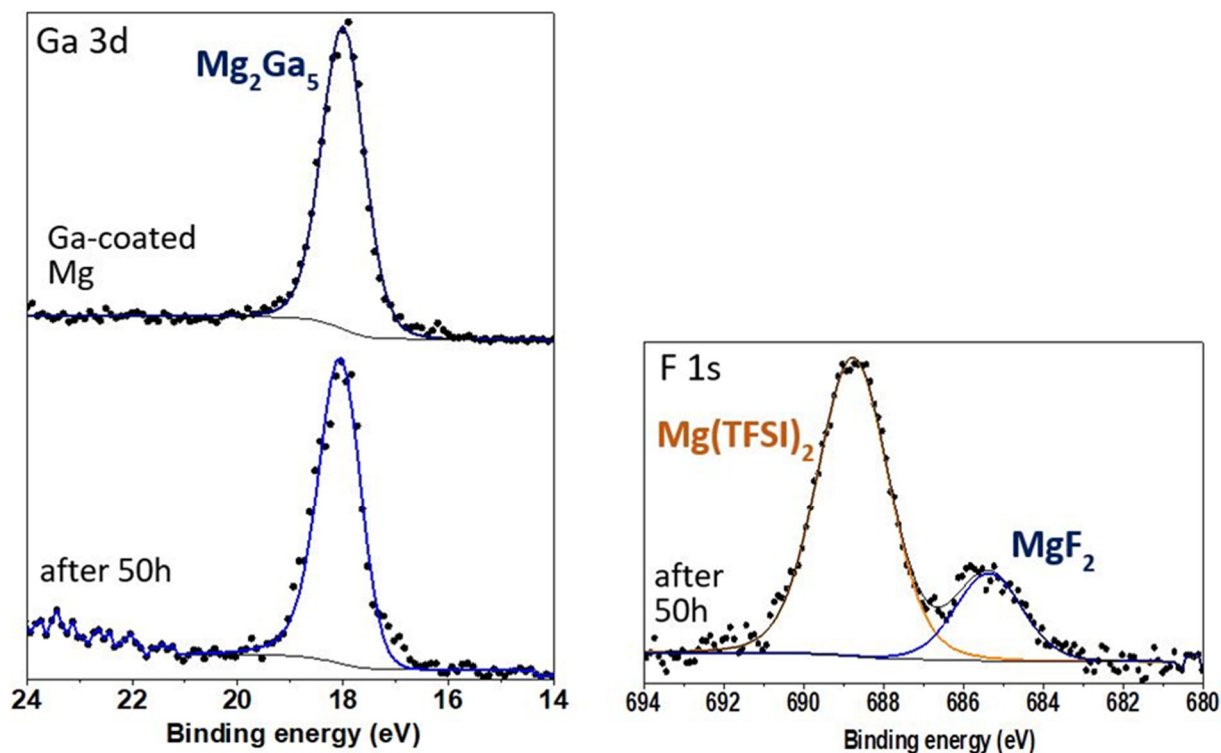


Figure S8. Ga 3d and F 1s XPS spectra of pristine Ga-coated magnesium electrode before and after 50 hours of plating/stripping measurements in symmetric cell.

Synthesis and characterization of Chevrel phase Mo_6S_8 . The synthesis protocol is adapted following the work of Choi *et al.*¹³ Firstly $\text{Cu}_{2.5}\text{Mo}_6\text{S}_8$ is prepared from stoichiometric amounts of Cu (99.9%, Alfa Aesar), MoS_2 (99%, Sigma-Aldrich) and Mo (99.95%, Alfa Aesar). The powders are ground together in Ar atmosphere with spex high-energy milling for 100 minutes. Then the mixture is heated in alumina crucible in tubular furnace under Ar flow for 24 hours at 1100 °C. Routine XRD pattern confirms the formation of the phase with no visible impurity. Secondly, the as-obtained powder immersed in acid solution for Cu removal (typically 6 hours in 50mL of 6mol/L HCl solution for 1 g of $\text{Cu}_{2.5}\text{Mo}_6\text{S}_8$ powder). The leached powder is then filtered and thoroughly wash with deionized water and finally ethanol, and finally allowed to dry for 1 night at 100°C under dynamic vacuum. Routine XRD pattern confirms the Cu removal and therefore the formation of Mo_6S_8 with refined cell parameters in agreement with the literature.

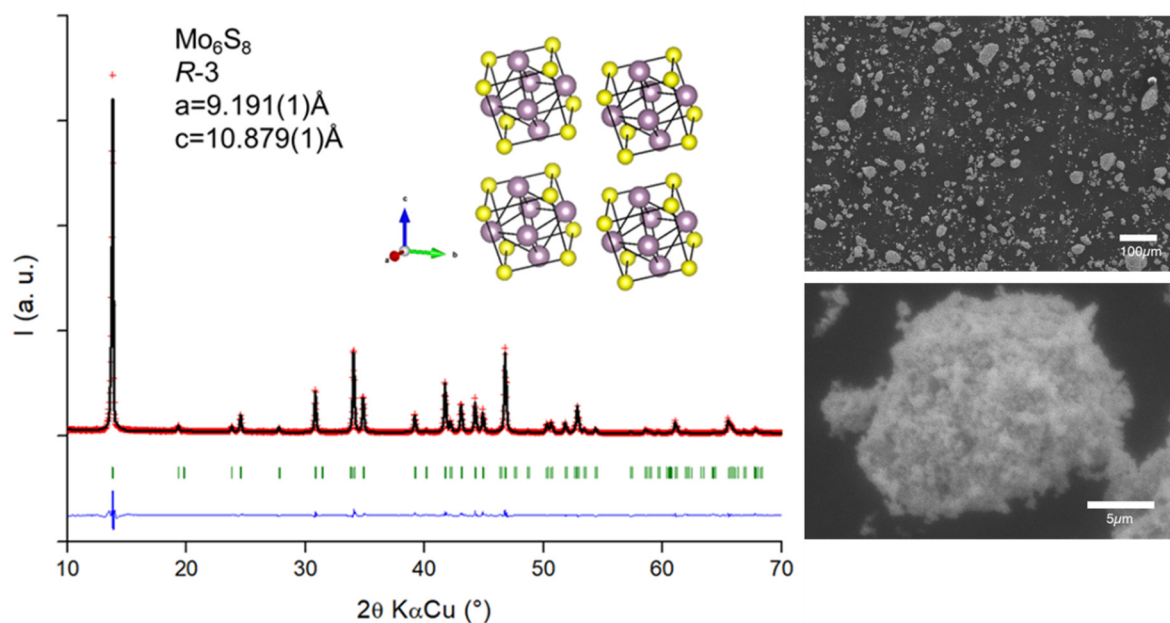


Figure S9: XRD pattern with profile matching refinement of Chevrel phase Mo_6S_8 powder and crystal structure in inset (Mo and S atoms are depicted in blue and yellow, respectively).

Synthesis, characterization and electrode formulation of Mg_2Ga_5 . Magnesium powder (98%, Sigma-Aldrich, reagent grade, 20–230 mesh) (and gallium pellets from Alfa-Aesar (6 mm diameter, 99.9999 % metal basis) have been mixed together in stoichiometric proportions during 5 hours in a SPEX 8000M 3D mill with stainless steel jars and balls in argon atmosphere. The resulting grey powder is then recovered, stored in argon-filled glovebox and characterized by X-ray diffraction. Phase identification confirms the formation of Mg_2Ga_5 intermetallic compound, with the following crystallographic parameters obtained through profile matching refinement: space group $I4/mmm$, $a = 8.656(1) \text{ \AA}$ and $c = 7.133(2) \text{ \AA}$.

Mg_2Ga_5 self-standing electrodes are prepared by mixing Mg_2Ga_5 powder with carbon (Super C65, Timcal) and PTFE binder (Sigma-Aldrich, 40 μm size) in the weight ratio 60 : 30 : 10. The as-obtained paste was then cut into 3-5 mm discs, for an average loading of 10 -30 mg/cm^2 . The Mg_2Ga_5 bulk electrodes are then evaluated versus Mo_6S_8 , ACC-S and PAQS-CNT cathode materials. In all cases, thanks to the high loading, Mg_2Ga_5 electrodes were more capacitive.

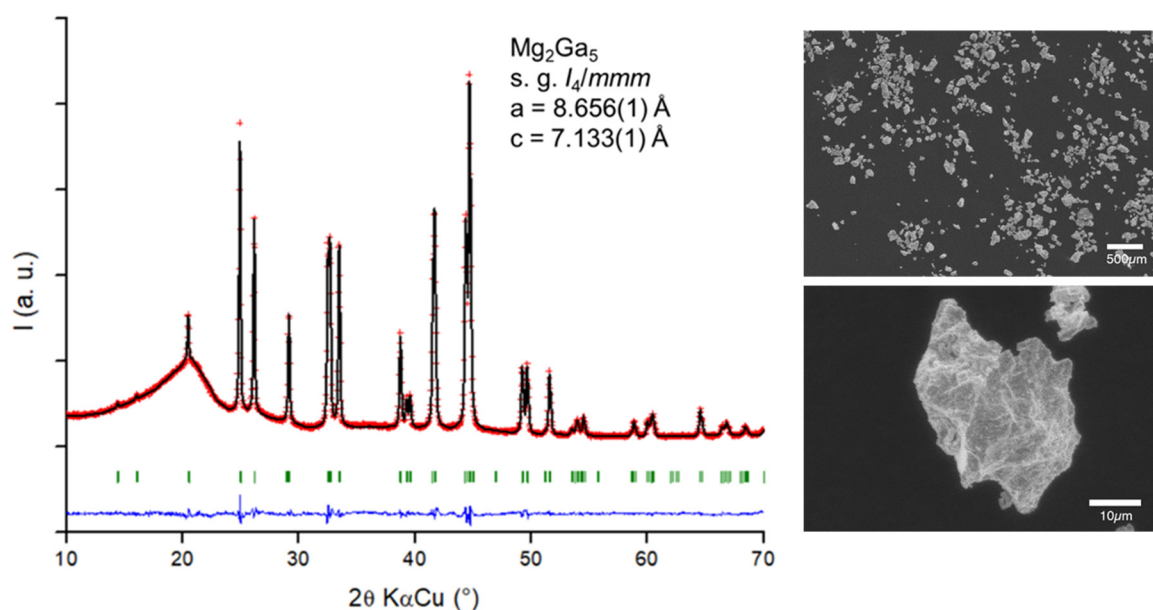


Figure S10: XRD pattern of Mg_2Ga_5 powder sample obtained by mechanical alloying, with profile matching refinement.

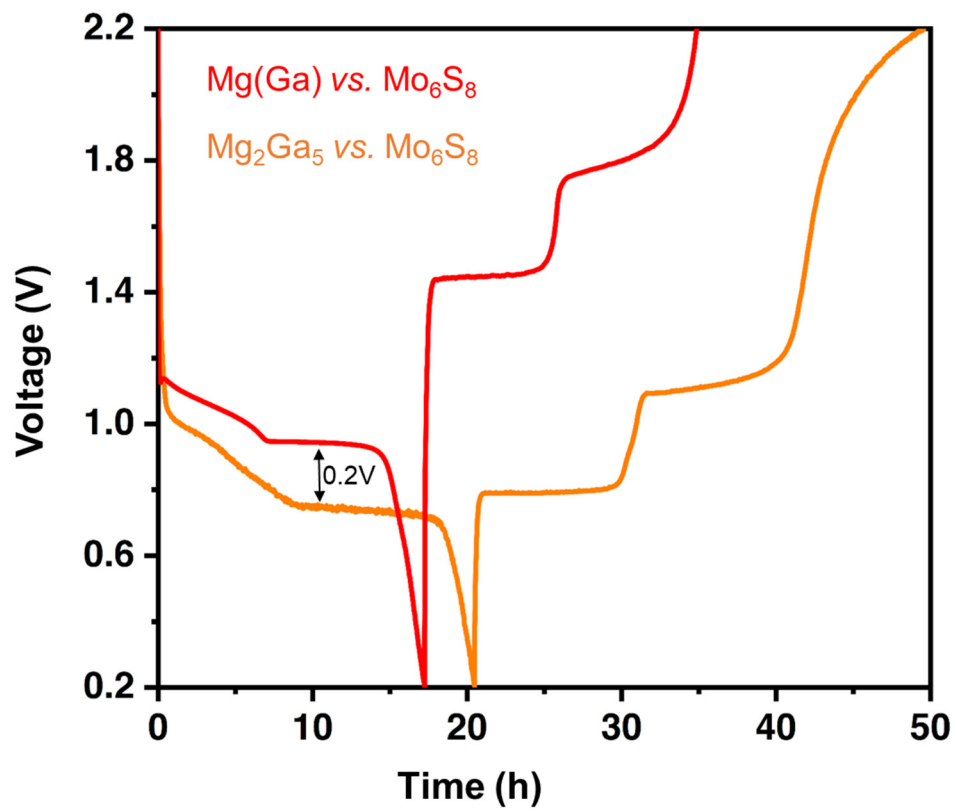


Figure S11: Comparison of the galvanostatic profiles obtained with Ga-treated Mg and Mg₂Ga₅ bulk electrodes versus Mo₆S₈ as cathode material.

Preparation of sulphur-carbon composite electrode. Sulphur positive electrodes were made by impregnation of sulphur inside an activated carbon cloth (ACC 507-20, Kynol Europa GmbH) following previous procedures.¹⁴⁻¹⁶ The ACC were first punched into disc of 8 mm diameter and then dried under vacuum at 120 °C for 4 h. Sulphur powder was spread on the surface of the ACC and put into a stainless steel autoclave under Ar. The autoclave was heated at 155°C for 16h with a rate of 0.2 °C/min. A second heat treatment at 200 °C for 50 min under flowing Ar was performed after cooling down to remove sulphur on the surface of the ACC fibres. The electrodes had an average loading of 1mg/cm².

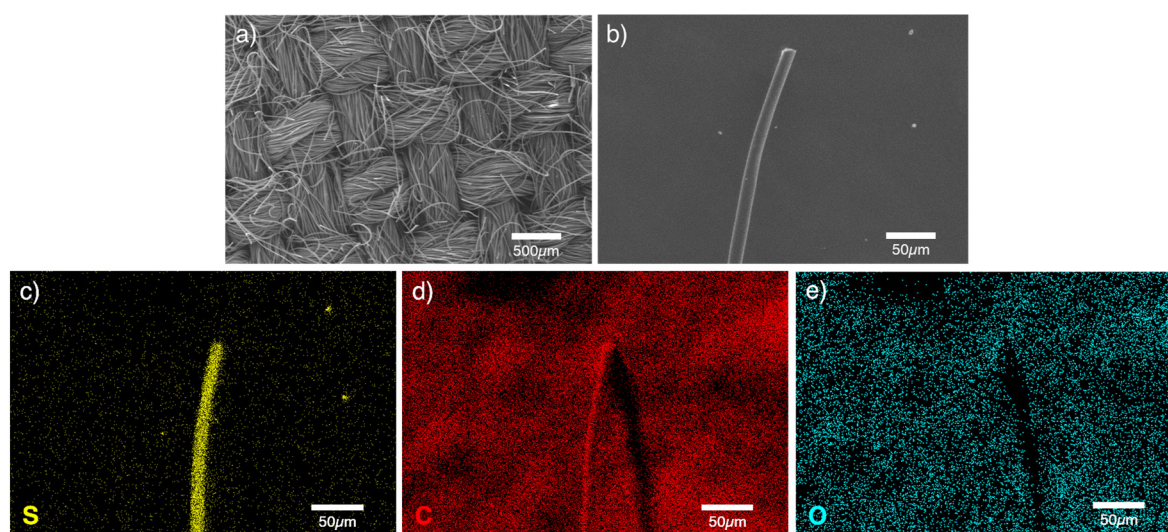


Figure S12: SEM images of ACC-S electrode with EDX mapping confirming the homogeneous distribution of sulphur along the carbon fibres.

Preparation of organic-carbon composite electrode. The anthraquinone-based polymer has been prepared following previous reports.^{17,18} All chemicals were of reagent grade and used as received, except $\text{Na}_2\text{S}\cdot x\text{H}_2\text{O}$ (Sigma Aldrich 13468) which was first dried by azeotropic dehydration using toluene till no water was collected anymore and then dried using vacuum pump overnight (50 °C). Multi-walled carbon nanotubes (0.595 g, Nano Tech Labs, C-grade) were dispersed inside 300 ml of N-methyl-2-pyrrolidone (NMP) using ultrasonic tip in ice bath. Then dried Na_2S (1.950 g, 25 mmol) and 1,5 – dichloroanthraquinone (6.93 g, 25 mmol, Alfa Aesar A19534) were added to NMP suspension of CNTs. Prepared solution was bubbled with nitrogen (20 mins.). Subsequently, reaction mixture was heated to 200 °C and left to react overnight under constant stirring and static nitrogen atmosphere. Afterwards, product was filtered and washed with hot water and acetone several times. Finally, product was dried at 120 °C for 12 h, obtaining 5.96 g of poly (anthraquinonyl sulphide) composite (PAQS-CNT). Composite electrodes were then made by mixing the as-obtained active material with carbon (Printex) and binder (PTFE) in the weight ratio 6:3:1 for a typical loading around 2-3 mg/cm².

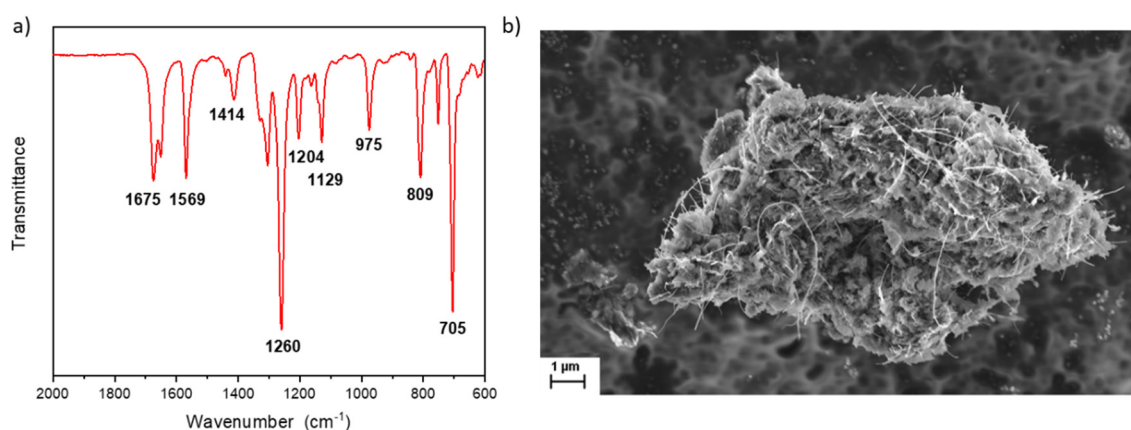


Figure S13: IR spectra and SEM image of PAQS. IR spectra was measured on FTIR spectrophotometer Bruker IFS66/S using KBr pellet. SEM was conducted on FE-SEM Supra 35 VP Carl Zeiss, at accelerating voltage of 3 kV with the use of InLens detector. The peak at 1675 cm⁻¹ corresponds to the stretching vibration of the C=O bond. The absorption at 1569 cm⁻¹ is assigned to the stretching vibration of the C=C bond in the aromatic ring. The peak at 1129 cm⁻¹ is assigned to ring-sulphur stretching, and the peak at 1414 cm⁻¹ is a consequence of ring stretching of the sulphur disubstituted aromatic ring.

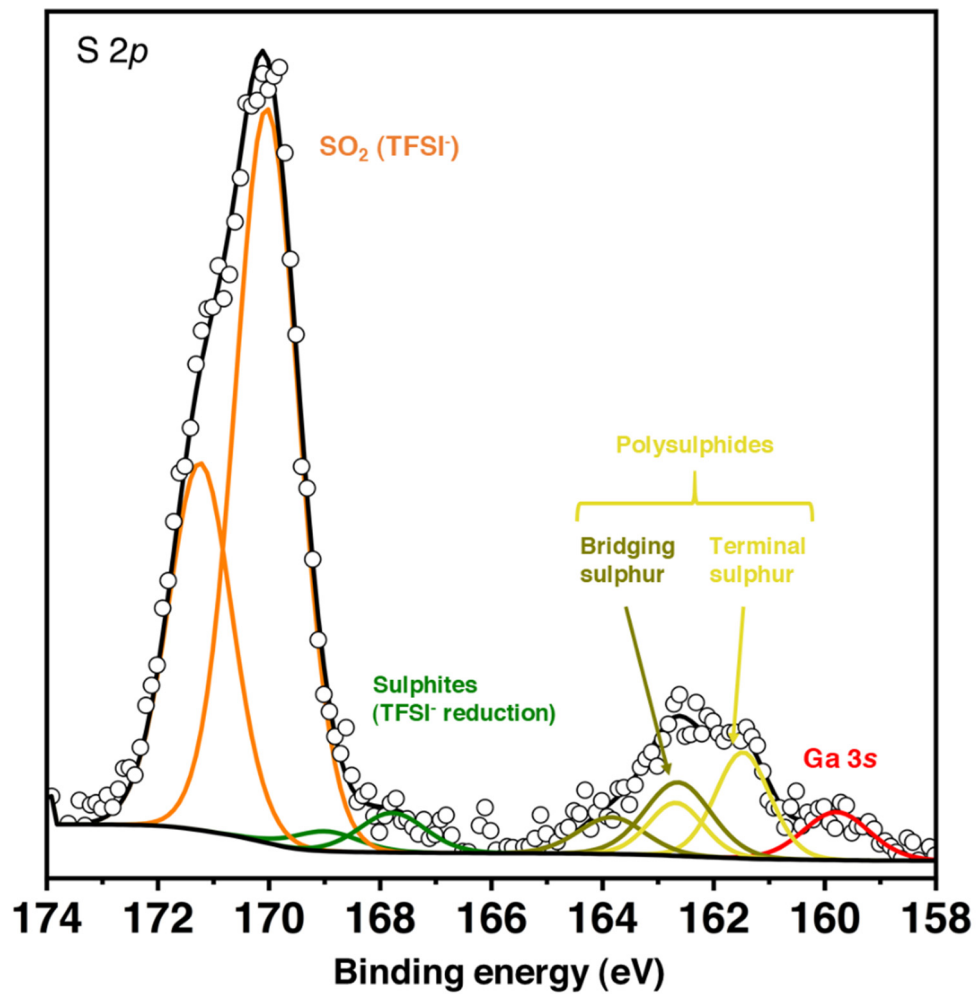


Figure S14. S 2p XPS spectrum of the Ga-coated electrode after 15 cycles of Mg(Ga)/ACC-S full cell, showing the presence of polysulphides species (with bridging and terminal sulphur atoms) at the surface of the negative electrode.

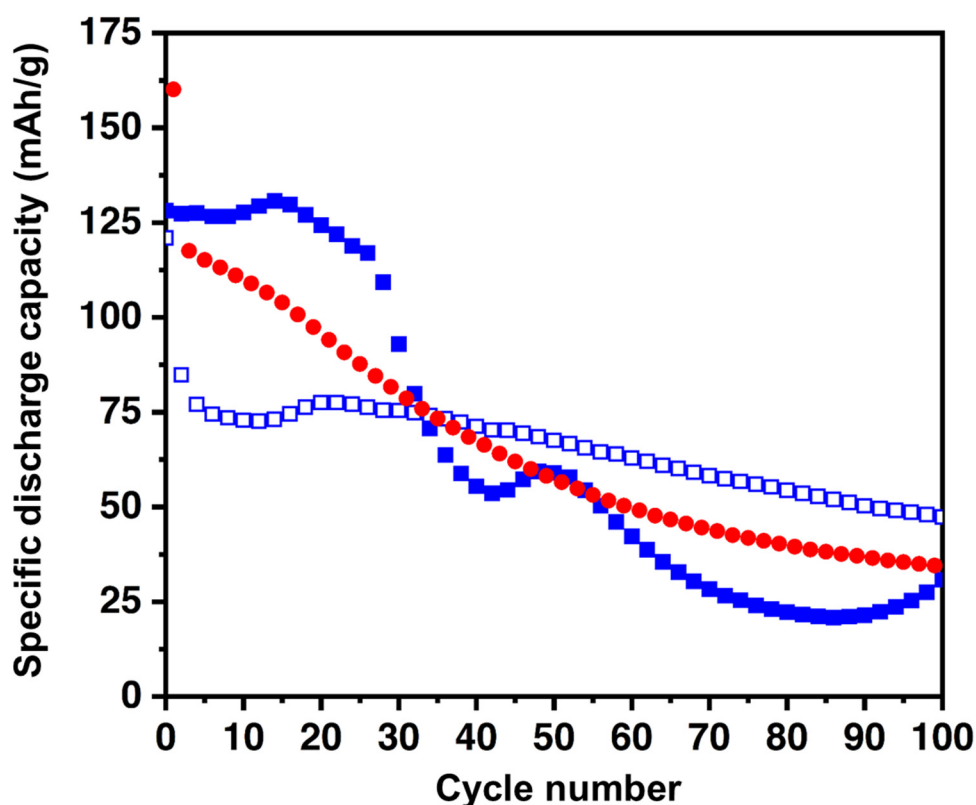


Figure S15: Capacity evolution of Mg(Ga)/PAQS-CNT using Mg(TFSI)₂/DME electrolyte (red circles) compare with Mg/PAQS-CNT using Mg(B(hfip)₄)₂ and Mg(TFSI)₂-2MgCl₂ electrolytes (plain and empty blue squares) and. For the two last electrolytes, electrochemical tests were performed in Swagelok type cells with stainless steel current collectors, and two GF/A Whatmann glassy fibre separators per cell. Cathodes were prepared by mixing the active material, carbon black (Printex XE2), and PTFE in ratio 6:3:1. Components were ball milled for 30 minutes at 300 rpm in suspension of isopropyl alcohol. After milling, the obtained slurry was rolled between two baking paper sheets and cut with a 12 mm disc puncher. Self-standing electrodes were obtained. For the counter electrode, brushed magnesium foil was used (12 mm diameter).

Energy density Calculation. This energy density calculation for Mg/S batteries is an approximation considering a 1cm² stack of electrodes without casing. The energy density is calculated by making the product of the sulphur loading, the sulphur capacity for a predetermine sulphur utilization, the average voltage observe for Mg/S in the literature, divided by the total mass or total volume of all cell components. The average voltage has been set to a realistic value of 1.5 V for Mg/S and Mg(Ga)/S and 1.3 V for the Mg₂Ga₅ bulk electrode. The E/S ratio and sulphur loading as been set according to the recommendation of Manthiram and coworkers¹⁹ with a realistic sulphur utilisation of 60%. A magnesium excess of 250 % is set for Mg electrode (uncoated or coated) and 100 % for Mg₂Ga₅ bulk electrode.

Specific energy density

$$m_{e-} = \frac{m_S \times C_S \times M_{Mg}}{F \times z}$$

$$m_C = \frac{m_S \times wt\%_C}{1 - wt\%_C - wt\%_B}$$

$$m_B = \frac{m_S \times wt\%_B}{1 - wt\%_C - wt\%_B}$$

$$m_{e+} = m_C + m_B + m_S + m_{Alcc}$$

$$m_E = V_E \times d_E$$

$$E_S = \frac{m_S \times V \times C_S}{m_{e-} + m_{e+} + m_E + m_{Sep}}$$

Volumetric energy density

$$V_{e+} = (V_S + V_B + V_C) \times P$$

$$E_V = \frac{m_S \times V \times C_S}{V_{e-} + V_{e+} + V_E + V_{Sep}}$$

m_S : Sulphur loading (mg/cm²)

m_{e-} : Mass of the negative electrode (mg/cm²)

m_C : Carbon loading (mg/cm²)

m_B : Binder loading (mg/cm²)

m_{e+} : Mass of the positive electrode (mg/cm²)

m_{Alcc} : Mass of the Al current collector (mg/cm²)

m_{Sep} : Mass of the separator (mg/cm²)

m_E : Mass of electrolyte (mg/cm²)

V : Average cell operating voltage (V)

C_S : Sulphur capacity (mAh/g)

E_S : Cell specific energy (Wh/Kg)

V_S : Sulphur volume (cm³)

V_B : Binder volume (cm³)

V_C : Carbon volume (cm³)

V_{e-} : Negative electrode volume (cm³)

V_{e+} : Positive electrode volume (cm³)

V_E : Electrolyte volume (cm³)

V_{sep} : Separator volume (cm³)

E_V : Cell volumetric energy (Wh/L)

Mg excess (-)	250 %
Mg ₂ Gas coating thickness	5, 10 and 20 μ m
Average operating voltage	1.5 V
Nature of the separator	Celgard
Porosity of the separator	39%
Nature of the electrolyte	Mg(TFSI) ₂ /DME
Concentration of the electrolyte	0.8M
E/S ratio	4
Nature of the current collector (+)	Al
Current collector thickness (+)	4 μ m
Electrode porosity (+)	20%
Active material loading	5mg/cm ²
Active material capacity	1675mAh/g
Active material utilization	60%
Carbon wt% (+)	20%
Binder wt% (+)	5%

Table S2: Parameters used in Figures S16 and S17 for the Mg and Mg(Ga) negative electrode configuration.

Mg excess (-)	100 %
Average operating voltage	1.3 V
Nature of the separator	Celgard
Porosity of the separator	39%
Nature of the electrolyte	Mg(TFSI) ₂ /DME
Concentration of the electrolyte	0.8M
E/S ratio	4
Nature of the current collector (+)	Al
Current collector thickness (+)	4 μ m
Nature of the current collector (-)	Al
Current collector thickness (-)	4 μ m
Active material loading	5mg/cm ²
Active material capacity	1675mAh/g
Electrode porosity (+ and -)	20%
Active material utilization	60%
Carbon wt% (+)	20%
Binder wt% (+)	5%
Carbon wt% (-)	20%
Binder wt% (-)	5%

Table S3: Parameters used in Figure S17 for the Mg₂Gas bulk negative electrode configuration.

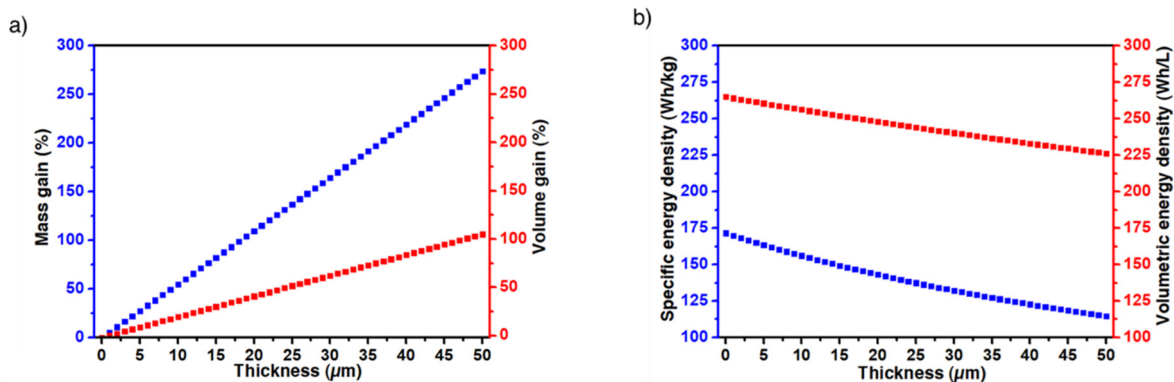


Figure S16: Evolution of a magnesium electrode mass and volume with an increasing thickness of the Ga-based coating (a) and corresponding evolution of specific and volumetric energy density (b).

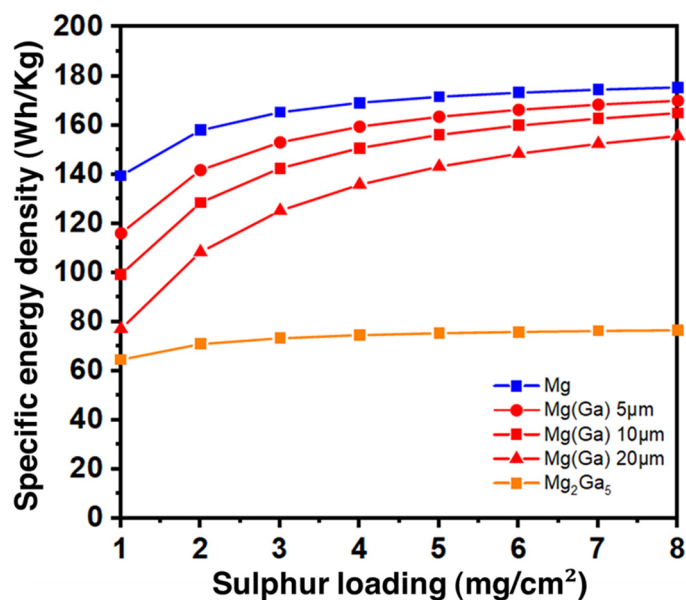


Figure S17: Estimation of the specific energy density of cells using: a bulk Mg_2Ga_5 anode, Mg anode protected with a $5\mu\text{m}$ Mg_2Ga_5 coating, Mg anode protected with a $10\mu\text{m}$ Mg_2Ga_5 coating, Mg anode protected with a $20\mu\text{m}$ Mg_2Ga_5 coating and bare Mg anode.

References

1. Son, S. B. *et al.* An artificial interphase enables reversible magnesium chemistry in carbonate electrolytes. *Nat. Chem.* **10**, 532–539 (2018).
2. Lv, R., Guan, X., Zhang, J., Xia, Y. & Luo, J. Enabling Mg metal anodes rechargeable in conventional electrolytes by fast ionic transport interphase. *Natl. Sci. Rev.* **7**, 333–341 (2020).
3. Zhang, J. *et al.* Rechargeable Mg metal batteries enabled by a protection layer formed in vivo. *Energy Storage Mater.* **26**, 408–413 (2020).
4. Zhao, Y. *et al.* A Bismuth-Based Protective Layer for Magnesium Metal Anode in Noncorrosive Electrolytes. (2021).
5. Li, Y. *et al.* Formation of an Artificial Mg²⁺-Permeable Interphase on Mg Anodes Compatible with Ether and Carbonate Electrolytes. (2021). doi:10.1021/acsami.0c22520
6. Zhang, R. *et al.* An artificial interphase enables the use of Mg(TFSI)₂-based electrolytes in magnesium metal batteries. *Chem. Eng. J.* **426**, 130751 (2021).
7. Kresse, G. & Hafner, J. Ab initio molecular dynamics for liquid metals. *Phys. Rev. B* **47**, 558–561 (1993).
8. Blöchl, P. E. Projector augmented-wave method. *Phys. Rev. B* **50**, 17953–17979 (1994).
9. Perdew, J. P., Burke, K. & Ernzerhof, M. Generalized Gradient Approximation Made Simple. *Phys. Rev. Lett.* **77**, 3865–3868 (1996).
10. Monkhorst, H. J. & Pack, J. D. Special points for Brillouin-zone integrations. *Phys. Rev. B* **13**, 5188–5192 (1976).
11. Mathew, K., Sundararaman, R., Letchworth-Weaver, K., Arias, T. A. & Hennig, R. G. Implicit solvation model for density-functional study of nanocrystal surfaces and reaction pathways. *J. Chem. Phys.* **140**, 84106 (2014).
12. Hagopian, A., Falcone, A., Ben Yahia, M. & Filhol, J.-S. Ab initio modelling of interfacial electrochemical properties: beyond implicit solvation limitations. *J. Phys. Condens. Matter* **33**, 304001 (2021).
13. Choi, S.-H. *et al.* Role of Cu in Mo₆S₈ and Cu Mixture Cathodes for Magnesium Ion Batteries. *ACS Appl. Mater. Interfaces* **7**, 7016–7024 (2015).
14. Gao, T. *et al.* Reversible S₀/MgS_x Redox Chemistry in a MgTFSI₂/MgCl₂/DME Electrolyte for Rechargeable Mg/S Batteries. *Angew. Chemie* **129**, 13711–13715 (2017).
15. Gao, T. *et al.* Thermodynamics and Kinetics of Sulfur Cathode during Discharge in MgTFSI₂ -DME Electrolyte. *Adv. Mater.* **30**, (2018).
16. Meng, Z. *et al.* Alloys to Replace Mg Anodes in Efficient and Practical Mg-Ion/Sulfur Batteries. *ACS Energy Lett.* **4**, 2040–2044 (2019).
17. Song, Z., Zhan, H. & Zhou, Y. Anthraquinone based polymer as high performance cathode material for rechargeable lithium batteries. *Chem. Commun.* 448–450 (2009). doi:10.1039/B814515F
18. Bitenc, J. *et al.* Anthraquinone-Based Polymer as Cathode in Rechargeable Magnesium Batteries. *ChemSusChem* **8**, 4128–4132 (2015).
19. Bhargav, A., He, J., Gupta, A. & Manthiram, A. Lithium-Sulfur Batteries: Attaining the Critical Metrics. *Joule* **4**, 285–291 (2020).